Relaxation of thermal stress by dislocation motion in passivated metal interconnects

Lucia Nicola[1], Erik Van der Giessen[1], Alan Needleman[2]

[1]The Netherlands Institute for Metals Research/

Dept. of Applied Physics, University of Groningen, Nyenborgh 4, 9747 AG Groningen, The Netherlands

[2]Division of Engineering, Brown University, Providence, RI 02912, USA

Abstract

The development and relaxation of stress in metal interconnects strained by their surroundings (substrate and passivation layers) is predicted by a discrete dislocation analysis. The model is based on a two-dimensional plane strain formulation, with deformation fully constrained in the line direction. Plastic deformation occurs by glide of edge dislocations on three slip systems in the single crystal line. The substrate and passivation layers are treated as elastic materials, and therefore impenetrable for the dislocations. Results of the simulations show the dependence of the stress evolution and of the effectiveness of plastic relaxation on the geometry of the line. The dependence of stress development on line aspect ratio, line size, slip plane orientation, pitch length and passivation layer thickness are explored.

1 Introduction

The reliability of many integrated circuits depends on the failure resistance of metallic interconnects. Typical damage processes that can induce failure in interconnects are void formation and electromigration. These processes are strongly influenced by the stress in the lines that develops as a consequence of the thermal mismatch between the metallic lines and their surroundings. The aluminum and copper alloys used for metallization have coefficients of thermal expansion that differ significantly from that of the silicon substrate to which they are usually bonded. Since the interconnects undergo large temperature excursions during processing, and often during service, their thermo-mechanical response is of interest.

Residual stresses in interconnects have been experimentally determined by X-ray diffraction [1, 2] and by curvature measurements [3, 4, 5]. Experiments have shown that the presence of a passivation layer results in a triaxial stress state in the line [2, 3], a stress state that favors void

formation, and that the mechanical behavior of passivated lines strongly depends on their aspect ratio [1, 3]. A disadvantage of most experimental techniques is that they do not measure stress accurately in small geometries. Moreover, they only measure the average stress in the lines and do not capture stress gradients, which can be large in small confined geometries. Recently developed energy-filtered electron diffraction methods [6], however, may offer significant improvement in this regard. Numerical analyses based on conventional continuum constitutive characterizations have been used to predict stress evolution in the lines, with the interconnect mainly treated as an elastic [7, 8, 9] or an elastic-perfectly plastic material [1, 10]. A key limitation of such approaches is that they cannot account for the size dependence of plastic response in small confined volumes.

In our analyses, plastic deformation in the line is treated as resulting from the collective motion of discrete dislocations which allows stress concentrations and gradients associated with dislocations and dislocation patterns to be captured. Upon cooling from a stress free state, the interconnect is strained by its substrate and by the passivation layer. During thermal loading, the evolution of the stress in the line cross-section and the evolution of the dislocation structure are predicted. Lines with various aspect ratio are analyzed and the results show rather good qualitative agreement with experiments [1, 3] for lines with a small aspect ratio: the larger the aspect ratio, the more elastic the line behavior. The possibility of a size effect is investigated: when the line height or width is sufficiently small (less than 0.5μm) lines with the same aspect ratio but of different size can exhibit a different response. The influence of slip plane orientation, pitch length and passivation layer thickness on stress evolution are also investigated.

2 Problem formulation

We consider an infinitely long array of single-crystal lines, perfectly bonded to a semi-infinite substrate and covered by a planar passivation layer (see Fig. 1). In the two-dimensional model illustrated in Fig. 1 the evolution of the stress field and of the dislocation structure in the cross-section of the lines is studied, assuming plane-strain conditions in the direction along the lines. This configuration is particularly relevant for aluminum lines on a silicon substrate, capped with a silicon-nitride passivation layer. In this type of system, the relatively stiff substrate and passivation layer provide significant constraint on plastic flow in the line in directions perpendicular to the line axis.

In most calculations, a planar crystal is analyzed that is an idealization of an FCC single crystal orientation with the plane of deformation being the (110) plane, as illustrated in Fig. 2. In this orientation, dislocation loops can form that are extended in the line direction. In the limit of an infinitely long line (which is the plane strain limit), these dislocations are straight and of

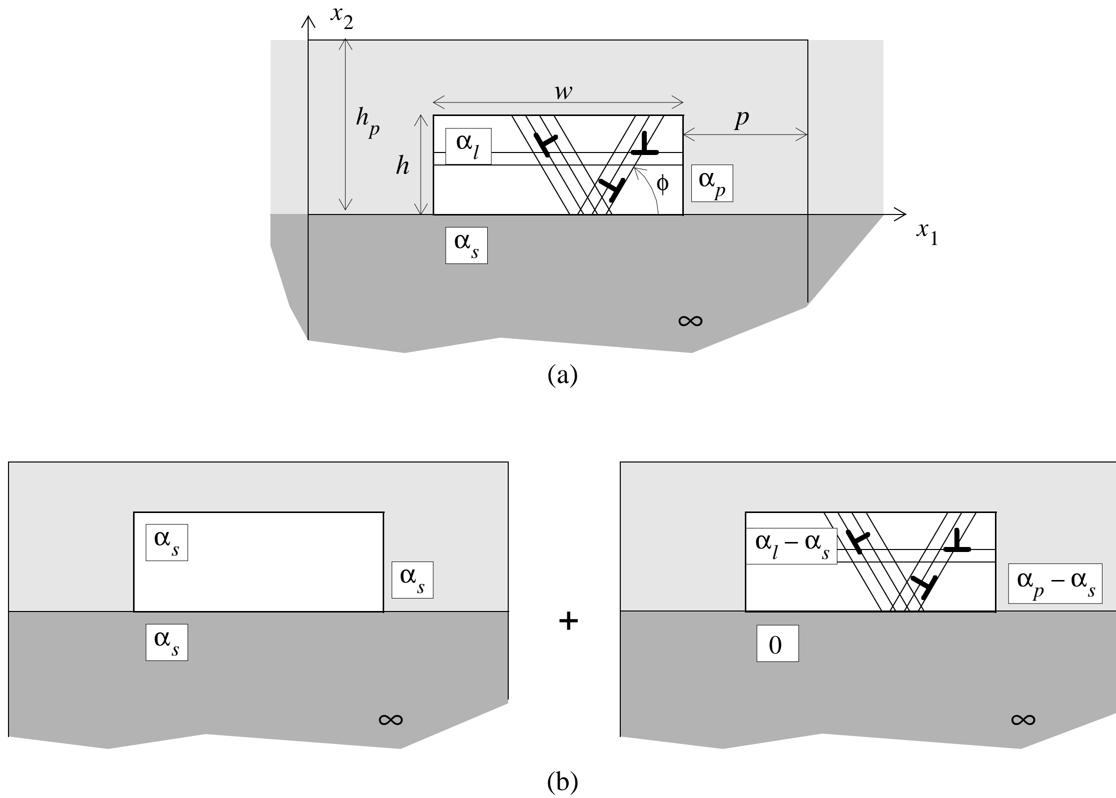

Figure 1: (a) Geometry of the line model. (b) Decomposition of the unit-cell problem into a thermo-elastic problem and a plastic relaxation problem.

edge character, [14]. Equal slip along the two face diagonals of the $(\bar{1}11)$ and $(1\bar{1}1)$ slip planes is consistent with the $[110]$ direction being perpendicular to the plane of deformation. Thus, slip on the $(\bar{1}11)$ plane (red in Fig. 2) effectively occurs in the $[1\bar{1}2]$ direction, while similarly on the $(1\bar{1}1)$ plane (green) slip effectively occurs in the $[\bar{1}12]$ direction. Another deformation possibility is slip in the $[110]$ direction on the (111) slip plane (blue). This does not correspond to a dislocation in the (110) plane (which therefore is dashed in Fig. 2), but since symmetry demands equal slip on the $(\bar{1}\bar{1}1)$ plane, the composition of these is equivalent to slip on the (001) plane. On the (110) plane the slip directions are therefore inclined at $\pm 54.7^\circ$ and 0° with the $[\bar{1}10]$ direction, which we identify with the x_1 axis.

In our plane strain analyses, we take the angles between slip directions to be near this FCC orientation and use three slip systems with the slip plane orientations: $\phi^{(1)} = 0^\circ$; $\phi^{(2)} = \phi^{(1)} + 60^\circ$; $\phi^{(3)} = \phi^{(2)} + 60^\circ$. This corresponds to $\phi = 60^\circ$ in Fig. 1 and we refer to this as the FCC-like orientation.

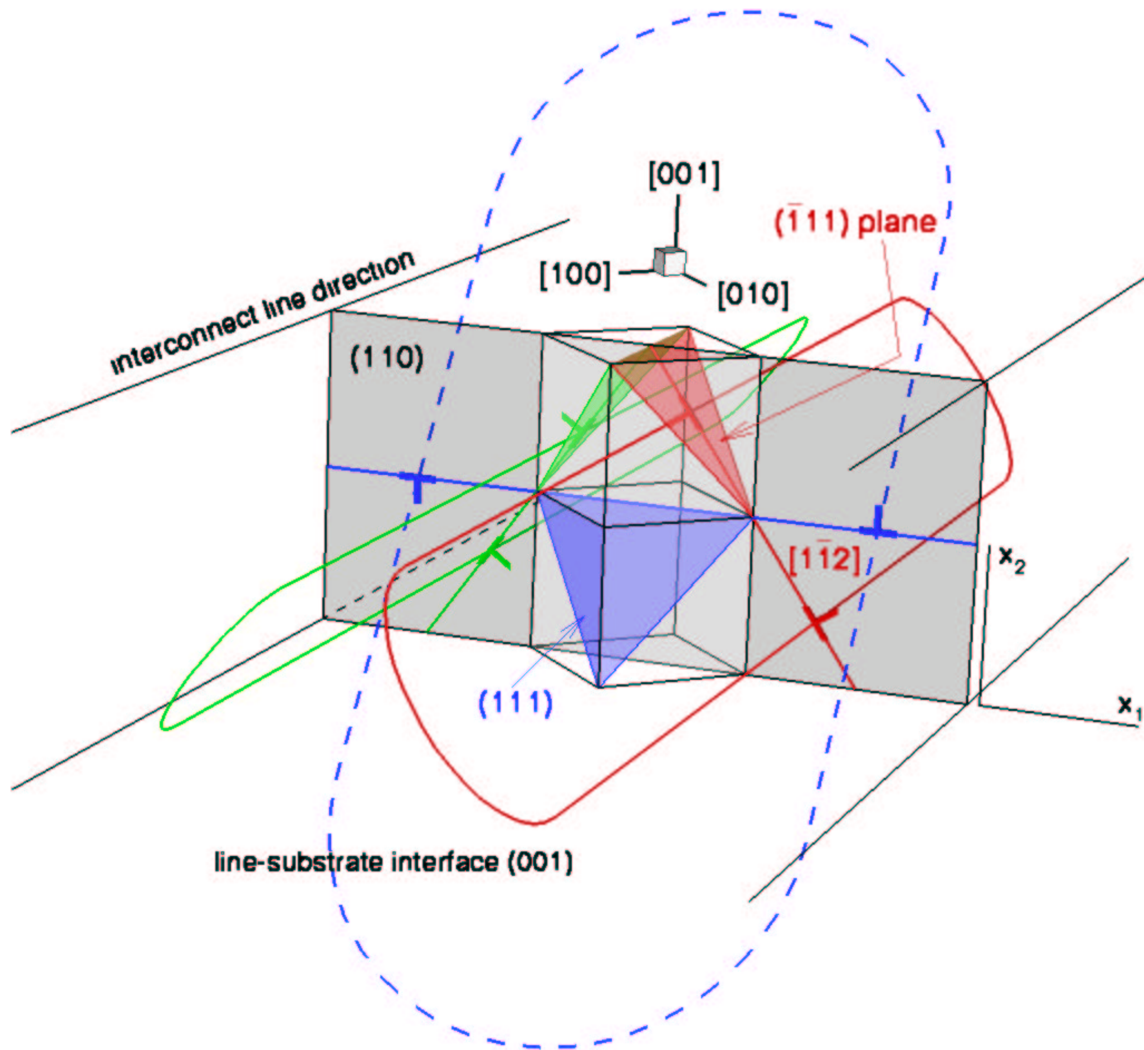

Figure 2: Schematic of dislocation motion on FCC slip planes when the crystal is oriented with [110] parallel to the line direction. Because of symmetry and when the line is very long, the slip mode is such that the dislocations can be idealized as three pairs of straight edge dislocations as shown by the $\perp$ symbols.

2.1 Boundary value problem

The analyses are carried out on a single cell of width $w+2p$, where w is the width of each line and $2p$ is the spacing (pitch) between lines, Fig. 1. In discrete dislocation plasticity, the fields in the line are obtained by coupling the solution of a boundary value problem for the single cell and the analytical solution for the dislocations, treated as line singularities in an infinite elastic medium (for more details see [11]).

The boundary value problem is defined by conditions of equilibrium and compatibility and

by the constitutive equations:

$$\sigma_{ij,j} = 0; \tag{1}$$

$$\varepsilon_{ij} = \frac{1}{2}(u_{i,j} + u_{j,i}); \tag{2}$$

$$\varepsilon_{ij} = \frac{1+\nu}{E}\left(\sigma_{ij} - \frac{\nu}{1+\nu}\delta_{ij}\sigma_{kk}\right) + \alpha\Delta T\delta_{ij}, \tag{3}$$

where σ_{ij} denotes the stresses, ε_{ij} the strains, u_i the displacements, ΔT is the temperature difference from the initial stress-free state, E is Young's modulus and ν is Poisson's ratio. The linear coefficient of thermal expansion of the line, the substrate and the passivation layer are denoted by α_l, α_s and α_p, respectively. Plane strain implies $\varepsilon_{i3} = 0, i = 1\ldots3$.

The problem is decomposed into two parts: an unconstrained thermo-elastic part, denoted by $(\ )^{\mathrm{th}}$ and a part that is driven by the thermal expansion mismatch, denoted by $(\ )'$ as shown in Fig. 1b. Their superposition provides the solution to the problem:

$$u_i = u_i^{\mathrm{th}} + u_i', \quad \varepsilon_{ij} = \varepsilon_{ij}^{\mathrm{th}} + \varepsilon_{ij}', \quad \sigma_{ij} = \sigma_{ij}^{\mathrm{th}} + \sigma_{ij}'. \tag{4}$$

The $(\ )^{\mathrm{th}}$ part treats the unconstrained thermal expansion of the system line-substrate-passivation layer, under the assumption that all components have the same coefficient of thermal expansion α_s. The solution is trivial. Since $\sigma_{ij}^{\mathrm{th}} = 0$ everywhere, dislocations are not involved in the solution of the $(\ )^{\mathrm{th}}$ part.

In the $(\ )'$ part of the problem, the thermal expansion coefficients of the substrate and passivation layers are taken to be α_s=α_p=0 and that of the line is $\alpha = \alpha_\mathrm{l} - \alpha_\mathrm{s}$. The $(\ )'$ part is subject to the following boundary conditions on the cell:

- stress-free surface

$$\sigma_{12}'(x_1, h_\mathrm{p}) = \sigma_{22}'(x_1, h_\mathrm{p}) = 0 \tag{5}$$

- periodicity conditions

$$u_i'(0, x_2) = u_i'(w + 2p, x_2). \tag{6}$$

When dislocations are present, the solution to the $(\ )'$ part is obtained by decomposing the fields as

$$u_i' = \hat{u}_i + \tilde{u}_i, \quad \varepsilon_{ij}' = \hat{\varepsilon}_{ij} + \tilde{\varepsilon}_{ij}, \quad \sigma_{ij}' = \hat{\sigma}_{ij} + \tilde{\sigma}_{ij}, \tag{7}$$

where the $(\tilde{\ })$-fields are the fields associated to the dislocations treated as individual dislocations in an infinite medium. The $(\tilde{\ })$-fields are given by the sum of the long-range fields of each dislocation in the cell (including their replicas in the periodic cells),

$$\tilde{u}_i = \sum_I u_i^{(I)}, \quad \tilde{\varepsilon}_{ij} = \sum_I \varepsilon_{ij}^{(I)}, \quad \tilde{\sigma}_{ij} = \sum_I \sigma_{ij}^{(I)}, \tag{8}$$

where the superscript (I) denotes the Ith dislocation. The $(\tilde{\ })$-fields are singular at the positions of the dislocations, and satisfy the standard equations of linear elasticity outside the dislocation core region. The $(\hat{\ })$-fields in (7) are the image fields which correct the $(\tilde{\ })$-fields in order to satisfy the boundary conditions (5) and (6) on the unit cell, cf. [11].

2.2 Rules for dislocation motion

The simulations are carried out using an incremental procedure: at each time step the temperature is changed by $\dot{T}\Delta t$, where $\dot{T}$ is the prescribed rate of temperature decrease and Δt is the time increment. The $(\ )'$ problem is solved and the dislocation structure is updated according to a set of constitutive rules [12]. In the calculations here we make use of the same three rules used in the previous study on thin films [13]:

- nucleation of a dipole from a point source occurs when the Peach-Koehler force on the source is larger than the nucleation strength $\tau_{\rm nuc} b$ during a time span $t_{\rm nuc} = 10$ ns. Such a point source is a two-dimensional representation of a Frank-Read source;
- dislocation glide is drag controlled: the velocity of a dislocation is proportional to the Peach-Koehler force acting on it through the drag coefficient $B = 10^{-4}$MPa, $v^{(I)} = B^{-1} f^{(I)}$;
- annihilation of a dipole occurs when the dislocations approach each other within the annihilation distance $L_{\rm e} = 6b$.

The Peach-Koehler force on dislocation I is given by

$$f^{(I)} = m_i^{(I)} \left(\hat{\sigma}_{ij} + \sum_{J \neq I} \sigma_{ij}^{(J)} \right) b_j^{(I)} ,$$

with $m_i^{(I)}$ the slip plane normal and $b_i^{(I)}$ the Burgers vector of dislocation I.

To accurately resolve dislocation-dislocation interactions, a small time step $\Delta t = 0.05$ns is needed. Therefore, to limit the computing time, the cooling rate is taken to be $\dot{T} = 40 \times 10^6$K/s which is much faster than experimental cooling rates.

3 Results and Discussion

We analyze the evolution of thermal stress in the line section while the temperature is decreased by 200K from a stress free and dislocation free state. The stress in the line arises from the thermal mismatch between the line, the substrate and the passivation layer. We take the thermal expansion coefficient of the line to be representative of aluminum, $\alpha_{\rm l} = 23.2 \times 10^{-6}$/K,

and use a value representative of silicon, $\alpha_s = 4.2 \times 10^{-6}$/K, for the substrate. In practice, aluminum lines on silicon substrates are usually passivated by silicon-nitride, which has a coefficient of thermal expansion that is very close to that of silicon; hence, in our calculations we take $\alpha_p = 4.2 \times 10^{-6}$/K. Moreover, for the lines, the elastic properties for aluminum are specified by $E = 70$GPa and $\nu = 0.3$. As in our previous analysis [13] of thin films, differences in elastic properties are neglected, so that the same elastic constants are used for the substrate and passivation layers.

As in our thin film study [13], Frank-Read sources are placed at random positions on the slip planes. The source density in all simulations is $\rho_{nuc} = 60/\mu m^2$. Hence, only some of the slip planes in the line are potentially active. The source strength is taken to be $\tau_{nuc} = 25$ MPa. The interfaces with substrate and passivation layer are modeled as impenetrable. Sources are not placed closer to these interfaces than the nucleation distance L_{nuc}: when a dipole is generated, both dislocations must be contained in the line. This implies that there is a zone of thickness $L_{nuc} \sin\phi$ around the line edges that is source free, independent of the line size.

The finite element mesh used to solve for the $(\hat{\ })$ fields is based on bilinear displacement four-node rectangular elements. A refined mesh is used inside the line, specially around the line corners. The mesh is gradually coarsened in the substrate with the mesh spacing increasing with distance from the line. The number of elements and degrees of freedom depend on the line size, with the meshes used consisting of from 48 to 252 elements inside the line.

3.1 Shape effects

All simulations start from a stress and dislocation-free state. As the temperature is decreased, an inhomogeneous stress state develops in the line, with the stress distribution and magnitude depending on the geometry of the line and of the passivation layer. The characteristics of the elastic stress field are key for the relaxation behavior. Therefore, we first present elastic simulations for four lines with various aspect ratios h/w. We take the line height to be constant, $h = 0.5\mu$m, and the line width to vary between $w = 0.25$ and $w = 2\mu$m, so that the aspect ratio ranges from $h/w = 0.25$ to $h/w = 2$ (see Fig. 1). In order to keep the line area fraction the same for the four lines, the ratio of passivation layer thickness to line height and the ratio of pitch $2p$ to line width w are fixed at $h_p/h = 2$ and $2p/w = 1$, respectively.

Figure 3 shows the distribution of σ_{11}, the stress parallel to the line-substrate interface, in the four lines after cooling by 200K. The line with $h/w = 0.25$ (Fig. 3a) is in a high, rather homogeneous tensile state with edge effects near the interfaces with the passivation layer. As h/w increases, Figs. 3b–d, the stress state changes such that σ_{11} in the core of the line is lower. High concentrations of stress are found close to the interface with the substrate and close to the top interface with the passivation layer. The compressive stress in the substrate is very small due

J. Mater. Res., **19** (2004), 1216–1226.

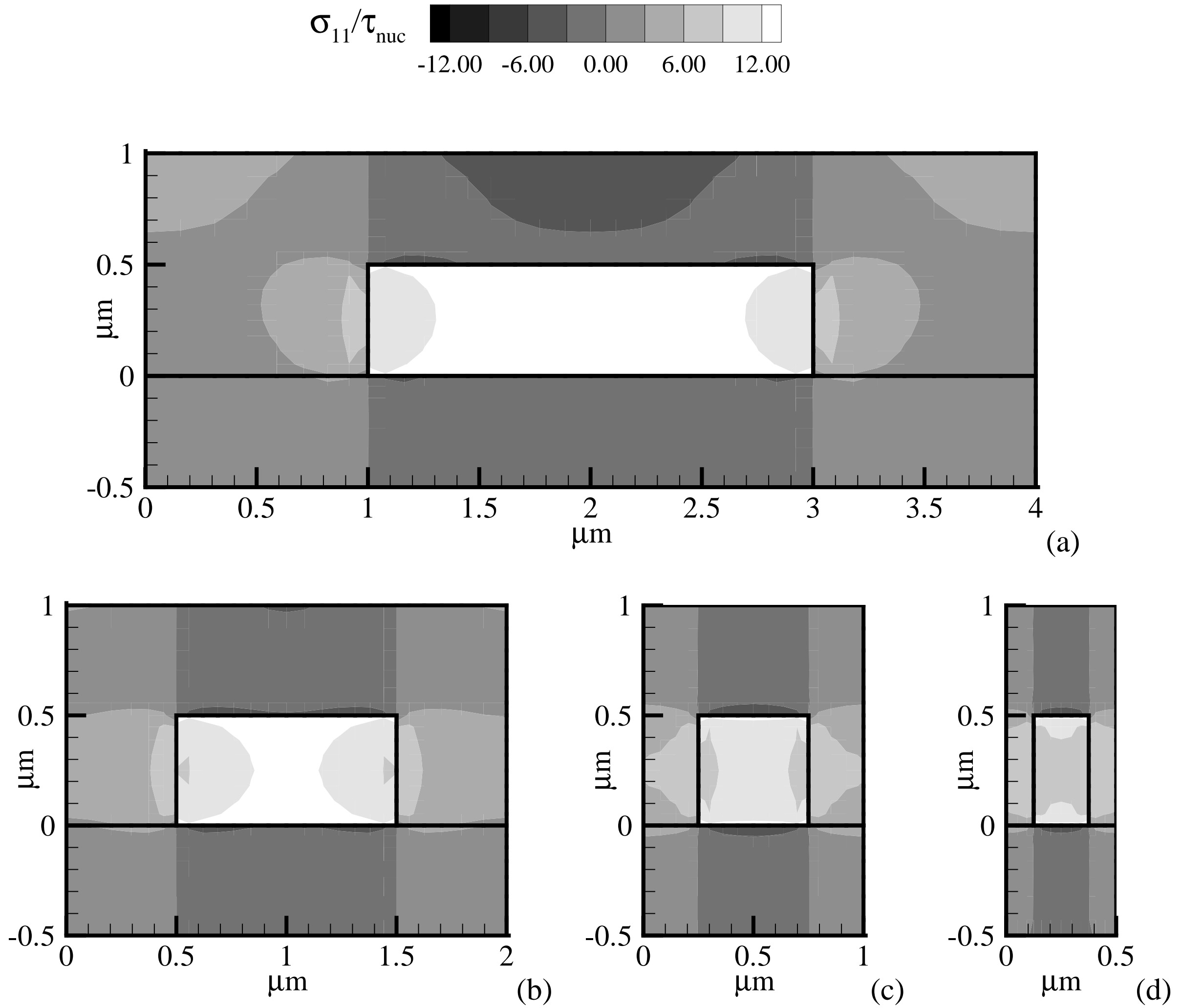

Figure 3: The elastic stress state. Contours of σ_{11}, normalized by the nucleation strength τ_{nuc} for four lines of height $h = 0.5\mu$m with various aspect ratios: (a) $h/w = 0.25$, (b) $h/w = 0.5$, (c) $h/w = 1$ and (d) $h/w = 2$.

to the large size of the substrate. The passivation layer, on average, is in tension between lines, especially for the taller lines. Above the line, the passivation layer is on average in compression.

The effect of dislocation glide on stress evolution is investigated for the same line geometries. The initial response of the line is elastic. The σ_{11} field has the distribution shown in Fig. 3 which then, along with the slip plane orientation, determines which source is subjected to the highest resolved shear stress. When the Peach-Koehler force on one of the sources attains the nucleation strength during a period t_{nuc}, the first dipole is nucleated. After nucleation, dislocations move apart on their slip plane, and relax the stress in the line. If they do not meet other dislocations on their path, they glide until they reach the impenetrable interfaces. More dislocations are nucleated and as the dislocation density increases, junctions between crossing dislocations form. These junctions may act as obstacles for other dislocations, but may also

trigger dislocation nucleation from nearby sources. The stress field in the lines evolves due to continued cooling and to the nucleation and motion of dislocations.

Figure 4 shows the stress field σ_{11} in the lines at final temperature (400K), with the corresponding dislocation distribution superimposed. Many dislocations have nucleated in the lines

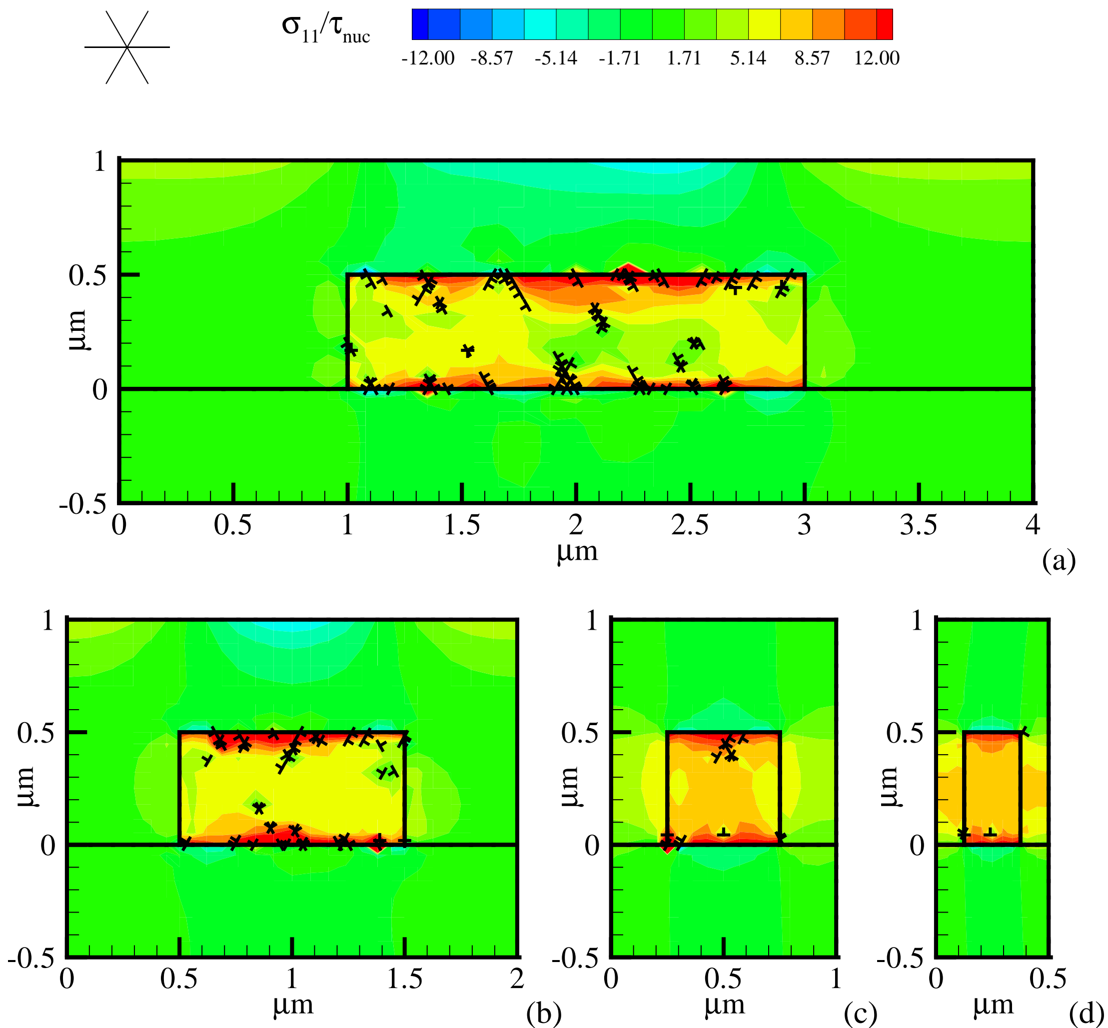

Figure 4: Relaxed state at final temperature. Contours of σ_{11}, normalized by the nucleation strength τ_{nuc}, and dislocation distribution for four lines of height $h = 0.5\mu$m with various aspect ratios: (a) $h/w = 0.25$, (b) $h/w = 0.5$, (c) $h/w = 1$ and (d) $h/w = 2$.

with aspect ratio $h/w < 1$ (see Figs. 4a and 4b) and have piled up at the top and at the bottom of the lines. Some dislocations have met other dislocations crossing their slip planes and have formed junctions in the cores of the lines. The dislocation activity in the lines with $h/w = 1$ and $h/w = 2$ is rather limited (see Fig. 4c and 4d). In the narrow line with aspect ratio $h/w = 2$ (Fig. 4d) only two dipoles have nucleated; the motion of these two dipoles does not significantly

affect the stress field inside the line, as can be seen by comparing Fig. 4d with Fig. 3d.

Figure 5 shows the evolution of the average stress in the line, $\langle\sigma_{11}\rangle$, during cooling. The stress-temperature curves for the four lines considered differ mainly in the elastic slope and in the onset of plasticity (dislocation activity starts earlier in lines with smaller aspect ratios). In lines with $h/w < 1$ the stress at yield is $\sigma_{11}^{y} \simeq 50$MPa for the parameters used in the calculations. The first dislocation nucleation is immediately followed by many other nucleation events, so that relaxation is very effective until $T \simeq 540$K, especially in the line with $h/w = 0.25$. Then, when the back stress associated with dislocation pile-ups formed at the interfaces becomes significant, the nucleation rate decreases and the material response becomes harder. This is similar to the findings in [13] for thin films, but even more pronounced due to the four-sided constraints on dislocation motion (note that the formation of long pile-ups is a consequence of the interfaces of the line with the passivation layer and with the substrate being modeled as impenetrable). In lines with $h/w \geq 1$ the yield strength is relatively high (in comparison with the nucleation strength $\tau_{\mathrm{nuc}} = 25$MPa); for $h/w < 1$: $\sigma_{11}^{y} \simeq 100$MPa with $h/w = 1$ and $\sigma_{11}^{y} \simeq 150$MPa with $h/w = 2$. The trend in these calculations is that stress relaxation by dislocation motion is more effective for smaller aspect ratio lines. Results presented in the following subsection show that this does not hold in general.

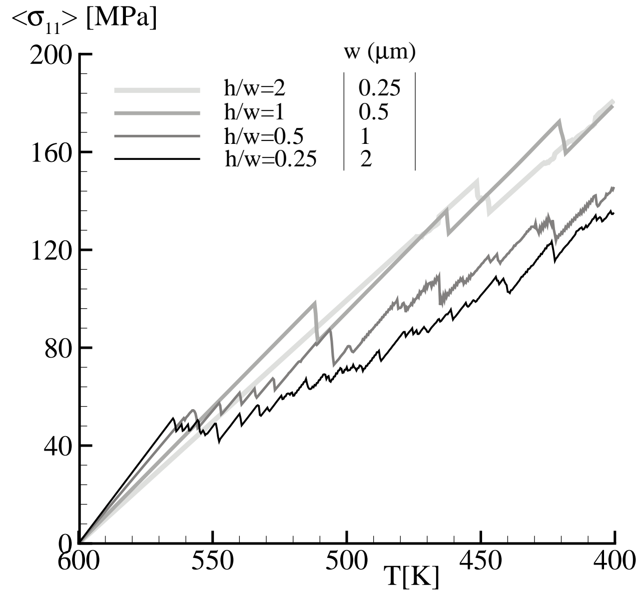

Figure 5: Average σ_{11} in the line versus imposed temperature for the four lines with aspect ratios shown in Fig. 4.

In order to understand why stress relaxation by dislocation motion is more effective for lines with $h/w < 1$, Fig. 6 shows the resolved shear stress at 60° in the four elastic lines normalized by the nucleation strength τ_{nuc}. In the line with $h/w = 2$ (Fig. 6d) there are only two very small

regions near the line corners where the resolved shear stress $\tau^{(2)}$ on the slip planes at $\phi^{(2)} = 60^\circ$ exceeds the nucleation strength. Only sources in these regions can nucleate dislocations. In flat lines, $h/w < 1$, the resolved shear stress magnitude is greater and distributed more homogeneously in the line, so that almost all sources available can be activated. It is also important to note that the small aspect ratio lines, $h/w < 1$, have more dislocation sources than the lines with $h/w \geq 1$; since h is fixed, lines with $h/w < 1$ have a larger cross-sectional area but the same source density as lines with $h/w > 1$.

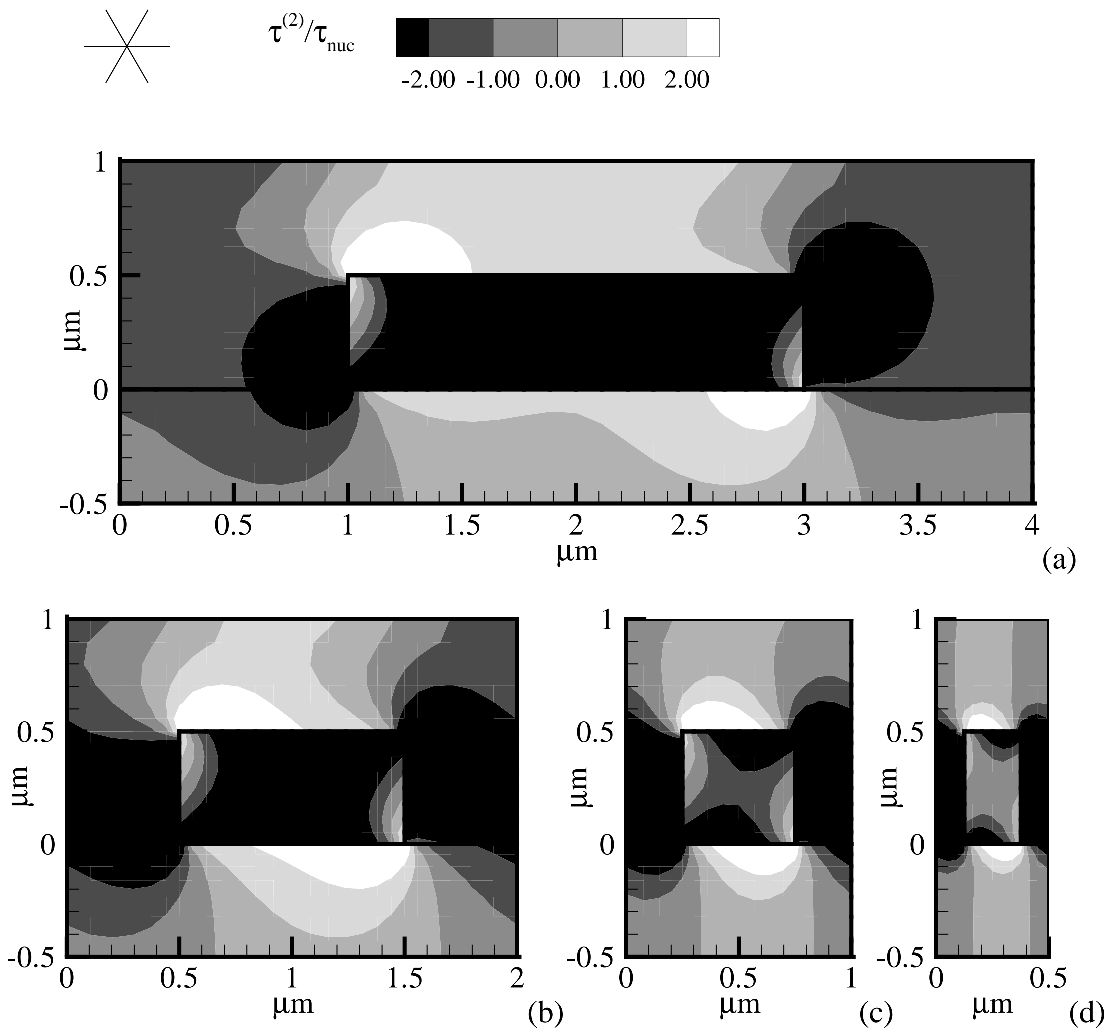

Figure 6: Distribution of the shear stress resolved on the slip planes at 60°, normalized by the nucleation strength τ_{nuc} for four lines of height $h = 0.5\mu$m with various aspect ratios: (a) $h/w = 0.25$, (b) $h/w = 0.5$, (c) $h/w = 1$ and (d) $h/w = 2$.

J. Mater. Res., **19** (2004), 1216–1226.

3.2 Size effects

To investigate the role of source availability on stress relaxation in the lines, we analyze a set of lines with varying aspect ratio but with the width fixed. The line width is now fixed at $w = 1\mu$m while the line height h ranges between 0.25μm and 1.5μm, so that the aspect ratio range remains between $h/w = 0.25$ and 1.5 for comparison with the previous results. The line area fraction is the same as in Fig. 3 and the elastic response of the lines is size independent. The use of a fixed width ensures that the ratio between the passivation layer thickness and the line height remains $h_{\mathrm{p}}/h = 2$ and the ratio between pitch and line width is still $2p/w = 1$. The σ_{11} stress and dislocation distributions at 400K are shown in Fig. 7. The line shown in Fig. 7a has the same aspect ratio ($h/w = 0.25$) as the line in Fig. 4a, but the cross-sectional area (0.25 μm^2) and the number of Frank-Read sources is the same as for the line in Fig. 4c. Despite the reduced number of sources (15 for the line in Fig. 7a versus 60 for the line in Fig. 4a), there is considerable dislocation activity and the stress in the line core has relaxed significantly. The availability of sources is greater in the present lines with $h/w \geq 1$, Figs. 7c and d, and the number of dislocations nucleated during the simulation is larger by a factor between 2 and 10 than for the lines in Figs. 4c, d. This is mainly due to the higher probability of a source being located in the zones with a high resolved shear stress. Nevertheless, despite the higher nucleation activity, stress relaxation in the lines has not been effective. This is seen in Fig. 8, where the average stress in the line, $\langle\sigma_{11}\rangle$, is plotted as a function of temperature. The response of lines with $h/w \geq 1$ is still almost elastic as in Fig. 5.

The inefficiency of relaxation for $h/w \geq 1$ is because the stress state in these lines is very close to being hydrostatic, as is shown in Fig. 9a, plotting $\langle\sigma_{11}\rangle$, $\langle\sigma_{22}\rangle$ and the average hydrostatic stress,

$$\langle\sigma_h\rangle = \frac{1}{3}[\langle\sigma_{11}\rangle + \langle\sigma_{22}\rangle + \langle\sigma_{33}\rangle], \quad (9)$$

in a line with $w = h = 1\mu$m. Figure 9b shows similar plots for a line with $h/w = 0.25$, $w = 2\mu$m and $h = 0.5\mu$m. The elastic stress in this flatter line is less hydrostatic, and $\langle\sigma_{11}\rangle$ is reduced, even though $\langle\sigma_{22}\rangle$ is not affected by dislocation glide. From Fig. 9a it seems that when dislocations nucleate, $\langle\sigma_{11}\rangle$ reduces but the transverse stress $\langle\sigma_{22}\rangle$ increases somewhat, thus maintaining the same hydrostatic stress state.

Taking a closer look at the dislocations in Figs. 4 and 7 one can see that lines with $h/w < 1$ are characterized by many dislocation pile-ups at the top and at the bottom of the lines. The magnitude of the net Burgers vector at the top of the line corresponds approximately to a super-dislocation with Burgers vector in the $-x_1$ direction. The dislocations at the bottom are equivalent to a super-dislocation with the opposite-signed Burgers vector. This dislocation structure is efficient in the relaxation of $\langle\sigma_{11}\rangle$, since it corresponds to the idealized picture of misfit dislocations at the top and at the bottom of the line. According to the same idealized picture,

relaxation of $\langle\sigma_{22}\rangle$ would require misfit dislocations at the line edges with their Burgers vector pointing in the x_2 direction on the left-hand edge and in the $-x_2$ direction on the other side. However, during the simulations, opposite net Burgers vectors develop on these sides. This observation emphasizes that a high dislocation density is not always effective in relaxing the stresses; what matters is the plastic straining, which depends on the distance that dislocations travel on the slip planes, and on the slip plane orientation. Dislocations on slip planes parallel to the line-substrate interface are not effective in relaxing $\langle\sigma_{11}\rangle$.

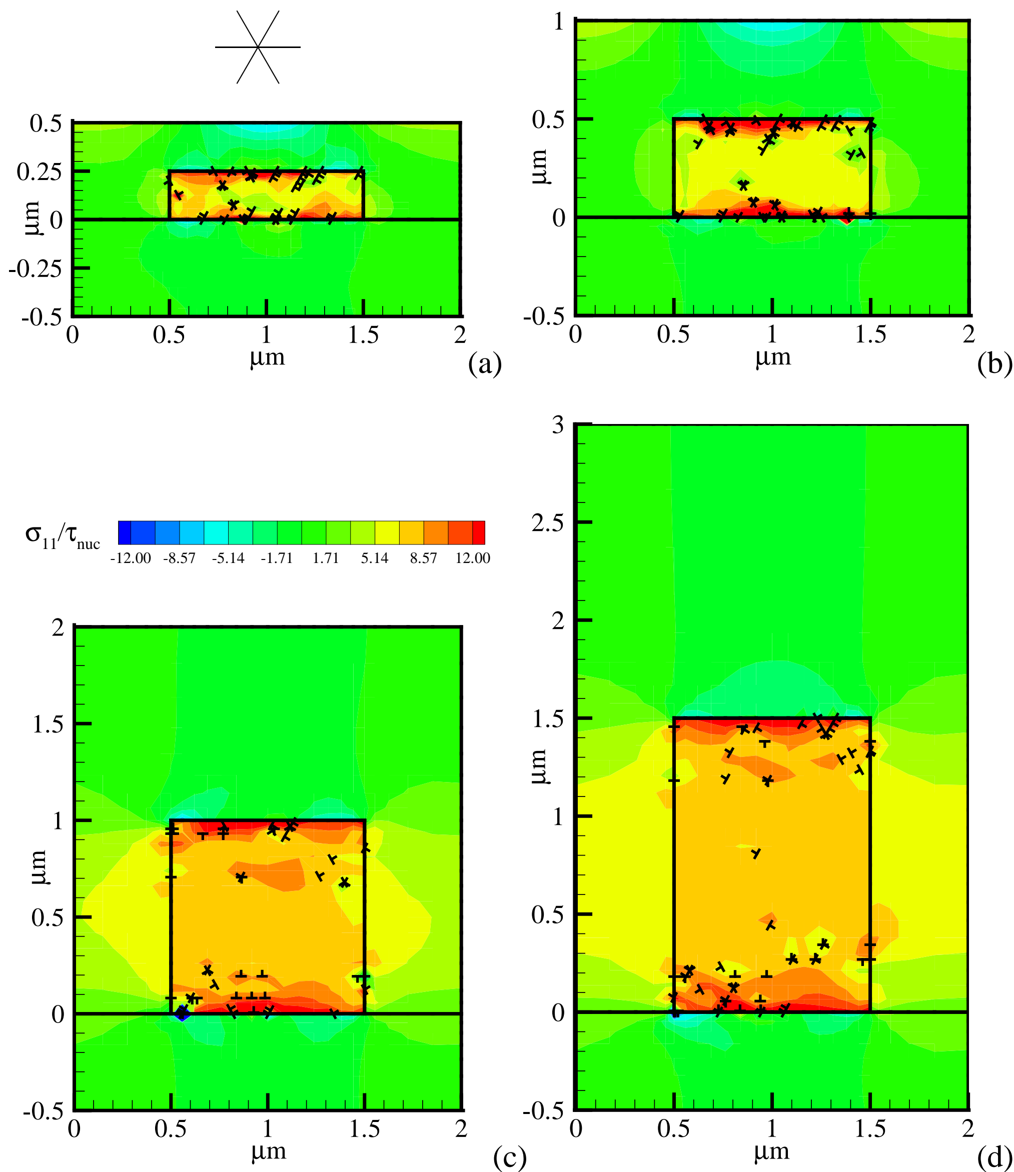

Figure 7: Contours of σ_{11}, normalized by the nucleation strength τ_{nuc} and dislocation distribution at final temperature for four lines of width $w = 1\mu m$ with various aspect ratios: (a) $h/w = 0.25$, (b) $h/w = 0.5$), (c) $h/w = 1$ and (d) $h/w = 1.5$.

J. Mater. Res., **19** (2004), 1216–1226.

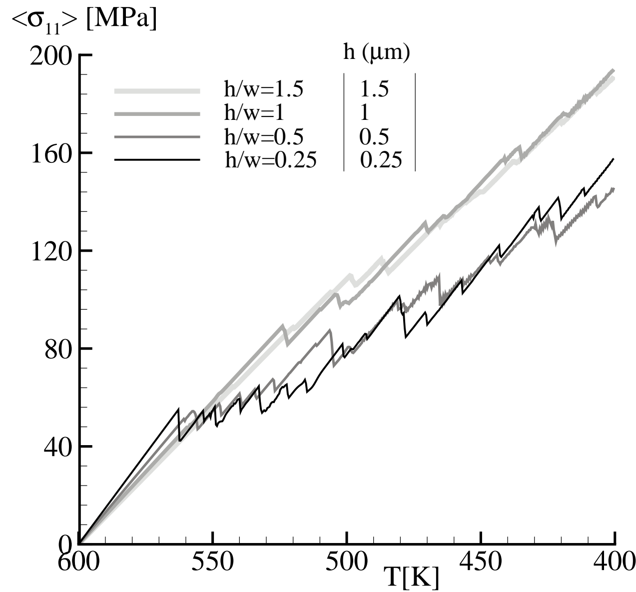

Figure 8: Average σ_{11} in the line versus imposed temperature for the four lines with width $w = 1\mu$m and aspect ratios: (a) $h/w = 0.25$, (b) $h/w = 0.5$, (c) $h/w = 1$ and (d) $h/w = 1.5$ of Fig. 7.

Comparison of Fig. 8 with Fig. 5 shows that the lines with $h/w = 0.25$ but of different size exhibit different hardening behaviors; the stress increase in the small line in Fig. 7a, after 560K, is higher than in the two times larger one in Fig. 4a. In fact, the $h/w = 0.25$ line in Fig. 8 hardens at least as fast the one with $h/w = 0.5$. One possible explanation is that the pile-ups which form in the line with $h = 0.25\mu$m are on average closer to the dislocation sources, so that their back stress inhibits nucleation. The back stress works against the formation and glide of new dislocations, which would make the pile-ups longer, and therefore hinders stress relaxation. This is similar to the size-dependent hardening mechanism seen in thin single-crystal films in [13]. Effective relaxation of $\langle\sigma_{11}\rangle$ for smaller aspect ratio lines, i.e. lines with $h/w < 1$, only occurs if the height of the line is large compared to the length of dislocation pile-ups. The width is not a limitation, because stress relaxation by glide is an effective mechanism only when $w > h$. In all the simulations with $w > h$ the average distance of dislocation sources from the top and the bottom of the lines is smaller than from the sides. Moreover, dislocation pile-ups rarely form at the lateral edges of the line.

3.3 Optimization

Since the hydrostatic stress plays a key role in void formation, it is of interest to reduce it as much as possible. We now consider only lines with $h/w < 1$, because relaxation of the $\langle\sigma_{11}\rangle$ stress is effective and because $\langle\sigma_{22}\rangle$ in these lines is smaller than $\langle\sigma_{11}\rangle$ (Fig. 9). The average

J. Mater. Res., **19** (2004), 1216–1226.

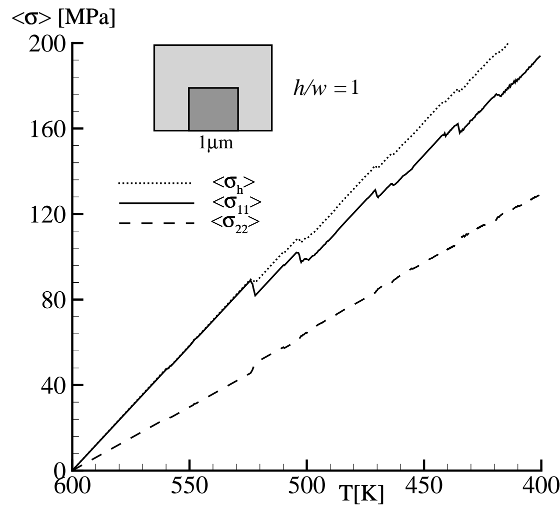

(a)

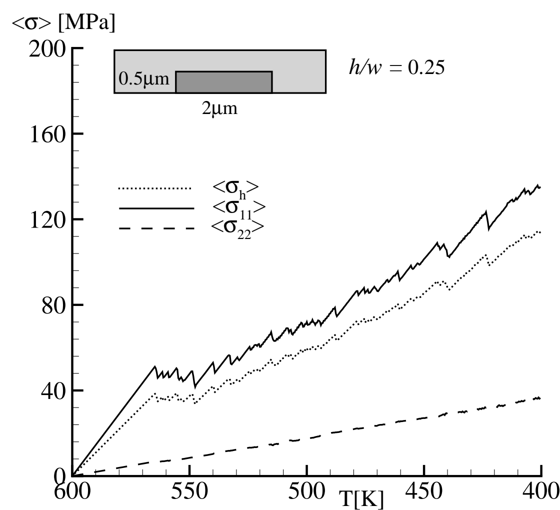

(b)

Figure 9: Average stress versus imposed temperature in lines with the same line area but with different aspect ratios: (a) $h/w = 1$; (b) $h/w = 0.25$.

hydrostatic stress in such lines at 400K is significantly lower than in lines with $h/w > 1$ but still around 120MPa.

3.3.1 Effect of slip plane orientation

More effective relaxation of $\langle\sigma_{11}\rangle$ is achieved by changing the slip plane orientation. In this Section, lines with slip planes oriented at $\phi^{(\alpha)} = (30^\circ, 90^\circ, 150^\circ)$ are considered which corresponds to a 30° rotation of the FCC-like orientation in the previous calculations. This can also

be considered as corresponding to a BCC-type orientation [14].

The calculation for the line with $h = 0.5\mu$m and $w = 2\mu$m is repeated in the rotated orientation. A comparison is given in Fig. 10 of the evolution of the average normal stresses $\langle\sigma_{11}\rangle$, $\langle\sigma_{22}\rangle$ and the hydrostatic stress $\langle\sigma_h\rangle$ for the two orientations. The line with the rotated orientation more effectively relaxes $\langle\sigma_{11}\rangle$: at 400K $\langle\sigma_{11}\rangle \simeq$ 90MPa for the BCC-type orientation while $\langle\sigma_{11}\rangle \simeq$ 140MPa for the FCC-type orientation. The number of dislocations piled-up at the top and at the bottom of the line in the BCC-type orientation is approximately the same as in the line with the FCC-type orientation, but, due to the orientation of their Burgers vector they are equivalent to $\sqrt{3}$ times more misfit dislocations than in the FCC-type crystal. The dislocation structure in the BCC-type crystal is more effective in relieving the $\langle\sigma_{11}\rangle$ stress. The BCC-type orientation is also slightly favorable for decreasing $\langle\sigma_{22}\rangle$ and the hydrostatic stress.

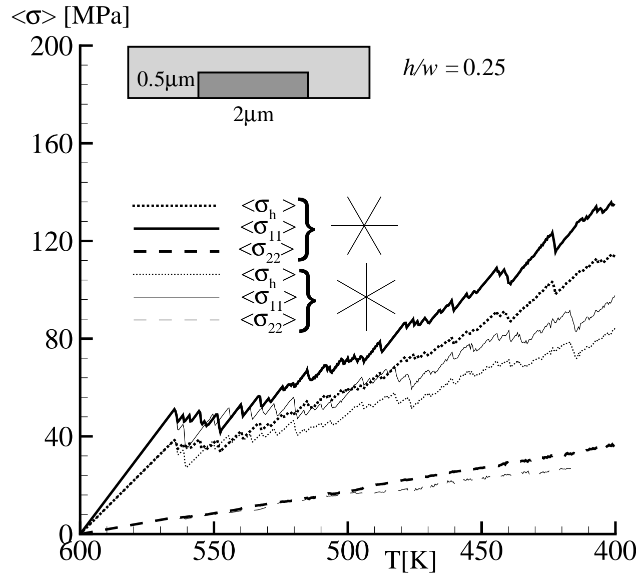

Figure 10: Average stresses versus imposed temperature in a line with aspect ratio $h/w = 0.25$ for FCC-type, $\phi^{(\alpha)} = (0°, 60°, 120°)$, and BCC-type, $\phi^{(\alpha)} = (30°, 90°, 150°)$, orientations.

3.3.2 Effect of a shorter pitch

In the calculation for the line with $h/w = 0.5$ ($h = 0.5\mu$m and $w = 1\mu$m), the pitch was $2p = 1\mu$m. We repeat this simulation keeping all the parameters fixed but changing the pitch to $2p = 0.5\mu$m. Neither the geometry of the line nor the number and position of sources are changed. Figure 11 shows a comparison of the average in-plane stress evolution in the two lines. When the lines are more closely spaced ($p = 0.25\mu$m) the hydrostatic stress is reduced in the elastic range. At the end of the simulation, at 400K, the average hydrostatic stress in the line with $p = 0.25\mu$m is

a little lower than in the line with $p = 0.5\mu$m. This is due to a reduced overall elastic stiffness against $\langle \sigma_{22} \rangle$ for the passivation layer which is a consequence of the change in geometry; as p decreases, the passivation layer between lines is narrower and this reduces the overall stiffness even though the elastic properties remain the same.

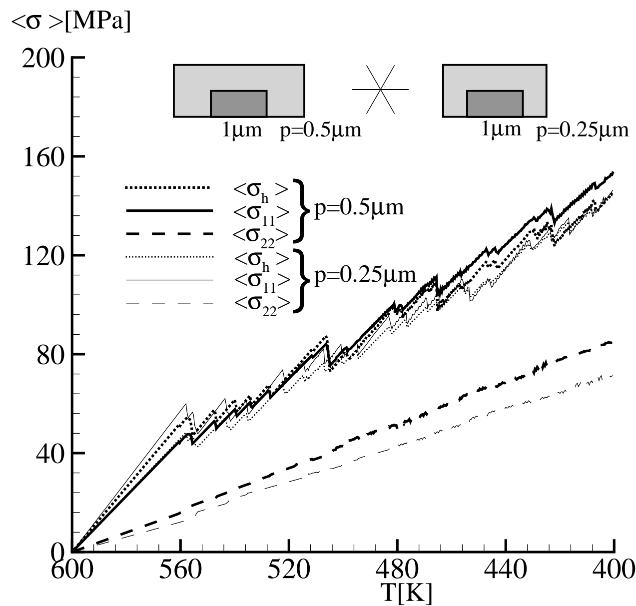

Figure 11: Average stresses versus imposed temperature in two lines with $w = 1\mu$m and $h = 0.5\mu$m which differ in the half-pitch: $p = 0.25\mu$m or $p = 0.5\mu$m.

3.3.3 Effect of a thinner passivation layer

The simulation for the line with aspect ratio $h/w = 0.5$ ($h = 0.5\mu$m and $w = 1\mu$m) is repeated with all parameters unchanged except for the height of the passivation layer, which is now $h_{\rm p} = 0.75\mu$m as compared with the previous value of $h_{\rm p} = 1\mu$m. Figure 12 shows that the stress state that develops in the line with the thinner passivation layer is slightly less hydrostatic than in the line with the thicker layer. The value of $\langle \sigma_{11} \rangle$ in the elastic range is the same in the two simulations, but because the hydrostatic component of the stress is reduced in the line with $h_{\rm p} = 0.75\mu$m, the resolved shear stress on the slip planes is increased and stress relaxation is slightly more efficient. In the elastic regime, the value of $\langle \sigma_{22} \rangle$ develops more slowly in the line with the thinner passivation layer. Thus, the average hydrostatic stress in the line is smaller if a thinner passivation layer is used.

J. Mater. Res., **19** (2004), 1216–1226.

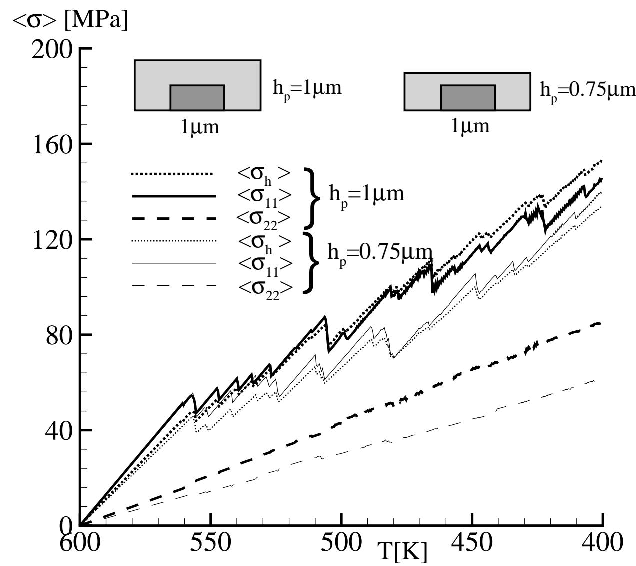

Figure 12: Average stresses versus imposed temperature in two lines with $w = 1\mu$m and $h = 0.5\mu$m for various heights of the passivation layer: $h_\mathrm{p} = 1\mu$m and $h_\mathrm{p} = 0.75\mu$m.

4 Conclusions

Discrete dislocation results have been presented on the evolution of thermal stresses in metal interconnects. A comparison of the mechanical response of lines characterized by the same cross-sectional area shows that:

- The stress that develops in lines with a height-to-width ratio near to or greater than one is nearly hydrostatic. As a consequence, plastic relaxation by dislocation motion is not effective in minimizing the internal stress in these lines.

- Lines with a height-to-width ratio that is significantly less then one develop a stress state that has a large deviatoric part so that substantial relaxation by dislocation motion occurs. The dislocations form pile-ups at the substrate and passivation layer interfaces, which give rise to hard boundary layers.

- Even if the height-to-width ratio is significantly less than one, plastic relaxation is inhibited if the height of the line is comparable to the dislocation nucleation length (the diameter of a stable loop nucleated from a Frank-Read source). In this case, the average distance of the sources to the line boundaries is small enough for the back stress associated with the boundary dislocation pile-ups to retard nucleation throughout the line.

- The effectiveness of plastic relaxation is orientation dependent. In the calculations here, plastic relaxation is more effective for crystals with $\phi^{(\alpha)} = (30°, 90°, 150°)$ (BCC-type)

J. Mater. Res., **19** (2004), 1216–1226.

than for crystals with $\phi^{(\alpha)} = (0^\circ, 60^\circ, 120^\circ)$ (FCC-type).

- A shorter pitch tends to reduce the hydrostatic stress in the line, because of a reduction in the stress parallel to the line-substrate interface.
- The difference between the thermal expansion coefficients of the substrate and the passivation layer, as well as the elastic mismatch between the line, the passivation layer and the substrate have been neglected in the calculations here. Accounting for these differences will alter the hydrostatic part of the elastic stress state and thereby the subsequent stress relaxation.

Acknowledgments

This research was carried out under project number MS97007 in the framework of the Strategic Research program of the Netherlands Institute for Metals Research in the Netherlands (www.nimr.nl). A.N. is pleased to acknowledge support from the Materials Research Science and Engineering Center on *On Micro-and-Nano-Mechanics of Electronic and Structural Materials* at Brown University (NSF Grant DMR-0079964).

J. Mater. Res., **19** (2004), 1216–1226.

References

[1] A. Saerens, P. Van Houtte, A. Witrouw, Internal stresses in aluminum interconnects, Mater. Sci. Forum, **347** (2000) 556–561.

[2] P.A. Flinn, C. Chiang, X-Ray diffraction determination of the effect of various passivations on stress in metal films and patterned lines, J. Appl. Phys., **67** (1990) 2927–2931.

[3] I.-S. Yeo, S.G.H. Anderson and P.S. Ho, Characteristics of thermal stresses in Al(Cu) fine lines. Passivated lines structures, J. Appl. Phys., **78** (1995) 953–961.

[4] A. Wikström, P. Gudmundson, Stresses in passivated lines from curvature measurements, Acta Mater. **48** (2000) 2429–2434.

[5] M.A. Moske, P.S. Ho, D.J. Mikalsen, J.J. Cuomo, R. Rosenberg, Measurement of thermal stress and stress relaxation in confined metal lines. Stresses during thermal cycling, J. Appl. Phys. **74** (1993), 1716–1724.

[6] S. Krämer, J. Mayer, C. Witt, A. Weickenmeier and M. Rühle, Analysis of local strain in aluminium interconnects by energy filtered CBED. Ultramicroscopy **81** (2000), 245–262.

[7] Y.-L. Shen, Modeling of thermal stresses in metal interconnects: effects of the aspect ratio, J. Appl. Phys., **82** (1997), 1578–1581.

[8] T.-S. Park, S. Suresh, Effects of line and passivation geometry on curvature evolution during processing and thermal cycling in copper interconnects lines, Acta Mater., **48** (2000) 3169-3175.

[9] P. Gudmundson, A. Wikström, Stresses in thin films and interconnect lines, Microelectron. Eng., **60** (2002), 17–20.

[10] A. Gouldstone, Y.-L. Shen, S. Suresh and C.V. Thompson, Evolution of stress in passivated and unpassivated metal interconnects, J. Mater. Res., **13** (1998), 1956–1966.

[11] E. Van der Giessen, A. Needleman, Discrete dislocation plasticity: a simple planar model, Modelling Simul. Mater. Sci. Eng. **3** (1995) 689–735.

[12] L.P. Kubin, G. Canova, M. Condat, B. Devincre, V. Pontikis and Y. Bréchet, Dislocation microstructures and plastic flow: a 3D simulation, Solid State Phenomena **23–24** (1992) 455–472.

[13] L. Nicola, E. Van der Giessen, A. Needleman, Discrete dislocation analysis of size effects in thin films, J. Appl. Phys. **93** (2003) 5920–5928.

J. Mater. Res., **19** (2004), 1216–1226.

[14] J.R. Rice, Tensile crack tip fields in elastic-ideally plastic crystals, Mech. Mater. **6** (1987) 317–335.

J. Mater. Res., **19** (2004), 1216–1226.

Figure Captions

Figure 1. (a) Geometry of the line model. (b) Decomposition of the unit-cell problem into a thermo-elastic problem and a plastic relaxation problem.

Figure 2 Schematic of dislocation motion on FCC slip planes when the crystal is oriented with $[110]$ parallel to the line direction. Because of symmetry and when the line is very long, the slip mode is such that the dislocations can be idealized as three pairs of straight edge dislocations as shown by the $\perp$ symbols.

Figure 3. The elastic stress state. Contours of σ_{11}, normalized by the nucleation strength $\tau_{\rm nuc}$ for four lines of height $h = 0.5\mu$m with various aspect ratios: (a) $h/w = 0.25$, (b) $h/w = 0.5$, (c) $h/w = 1$ and (d) $h/w = 2$.

Figure 4. Relaxed state at final temperature. Contours of σ_{11}, normalized by the nucleation strength $\tau_{\rm nuc}$ and dislocation distribution at final temperature for four lines of height $h = 0.5\mu$m with various aspect ratios: (a) $h/w = 0.25$, (b) $h/w = 0.5$, (c) $h/w = 1$ and (d) $h/w = 2$.

Figure 5. Average σ_{11} in the line versus imposed temperature for the four lines with aspect ratios shown in Fig. 4.

Figure 6. Distribution of the shear stress resolved on the slip planes at 60°, normalized by the nucleation strength $\tau_{\rm nuc}$ for four lines of height $h = 0.5\mu$m with different aspect ratios: (a) $h/w = 0.25$, (b) $h/w = 0.5$, (c) $h/w = 1$ and (d) $h/w = 2$.

Figure 7. Contours of σ_{11}, normalized by the nucleation strength $\tau_{\rm nuc}$ and dislocation distribution at final temperature for four lines of width $w = 1\mu$m with various aspect ratios: (a) $h/w = 0.25$, (b) $h/w = 0.5$), (c) $h/w = 1$ and (d) $h/w = 1.5$.

Figure 8. Average σ_{11} in the line versus imposed temperature for the four lines with width $w = 1\mu$m and aspect ratios: (a) $h/w = 0.25$, (b) $h/w = 0.5$, (c) $h/w = 1$ and (d) $h/w = 1.5$ of Fig. 7.

Figure 9. Average stress versus imposed temperature in lines with the same line area but with different aspect ratios: (a) $h/w = 1$; (b) $h/w = 0.25$.

Figure 10. Average stresses versus imposed temperature in a line with aspect ratio $h/w = 0.25$ for FCC-type, $\phi^{(\alpha)} = (0^\circ, 60^\circ, 120^\circ)$, and BCC-type, $\phi^{(\alpha)} = (30^\circ, 90^\circ, 150^\circ)$, orientations.

J. Mater. Res., **19** (2004), 1216–1226.

Figure 11. Average stresses versus imposed temperature in two lines with $w = 1\mu$m and $h = 0.5\mu$m which differ in the pitch: $p = 0.25\mu$m and (b) $p = 0.5\mu$m.

Figure 12. Average stresses versus imposed temperature in two lines with width $w = 1\mu$m and $h = 0.5\mu$m for various heights of the passivation layer: $h_\mathrm{p} = 1\mu$m and $h_\mathrm{p} = 0.75\mu$m.